Uniform momentum zone scaling arguments from direct numerical simulation of inertia-dominated channel turbulence

W. Anderson[1],† **and Scott T. Salesky**[2]

[1]Mechanical Engineering Department, The University of Texas at Dallas, Richardson, TX 75080, USA

[2]School of Meteorology, The University of Oklahoma, Norman, OK 73072, USA

Inertia-dominated wall-sheared turbulent flows are composed of an inner and outer layer, where the former is occupied by the well-known autonomous inner cycle while the latter is composed of coherent structures with spatial extent comparable to the flow depth. In arbitrary streamwise–wall-normal planes, outer-layer structures instantaneously manifest as regions of quasi-uniform momentum – relative excesses and deficits about the Reynolds average – and for this reason are termed uniform momentum zones (UMZs). By virtue of this attribute, the interfacial zones between successive UMZs exhibit abrupt wall-normal gradients in streamwise momentum; these interfacial gradients cannot be explained by the notion of attached eddies, for which the vertical gradient goes as $(x_3^+)^{-1}$ in the outer layer, where x_3^+ is inner-normalized wall-normal position. Using data from direct numerical simulation (DNS) of channel turbulence across inertial regimes, we recover vertical profiles of Kolmogorov length *a posteriori* and show that $\eta^+ \sim (x_3^+)^{1/4}$, thereby requiring that ambient wall-normal gradients in streamwise velocity must scale as $(x_3^+)^{-1/2}$. The data reveal that UMZ interfaces are responsible for these relatively larger wall-normal gradients. The DNS data afford a unique opportunity to interpret inner- and outer-layer structures simultaneously: we propose that UMZs – and the associated outer-layer dynamics – can be explained as the product of inner-layer bluff-body-like interactions, wherein wakes of quasi-uniform momentum emanate from the inner layer; wake-scaling arguments agree with observations from DNS.

Key words: turbulent mixing, turbulence theory

1. Introduction

The spatial attributes and energetic content of canonical turbulent wall flows are regulated by inertial conditions. Friction Reynolds number, $Re_\tau = u_\tau \delta \nu^{-1}$, is commonly used to define inertial conditions, where u_τ, δ and ν represent shear velocity, flow depth and kinematic viscosity, respectively. For sufficiently high Re_τ, turbulent channel flows are composed of a viscous inner (wall) region of thickness, $x_3^+ \simeq 50$ to 100, where '+' denotes an inner-scaled quantity, and an above logarithmic (inertial) region of thickness, $30 \lesssim x_3^+ \lesssim 2000$ (see also Pope 2000). The viscous inner region is occupied by a self-sustaining

† Email address for correspondence: wca140030@utdallas.edu

inner cycle of sinuous streaks (Jimenez & Pinelli 1999; Schoppa & Hussain 2002), which are enveloped by vortical hairpins due to interfacial shear (Adrian, Meinhart & Tomkins 2000). There are conceptual similarities in the vertical structure of turbulent channels, pipes and boundary layers, but the present work is posed in the context of channels only. Note that the viscous wall region resides within the inner layer, while the logarithmic region resides within the inner and outer layers in the so-called overlap region; further reading is available in Pope (2000). For $Re_\tau \gtrsim 2000$, energetic content appears in the outer layer due to the emergence of outer-layer streaks (Hutchins & Marusic 2007); substantial evidence of an inner–outer coupling has been provided in recent years (Marusic, Mathis & Hutchins 2010), although it is stressed that establishing dynamical hierarchy is not the focus of this article.

In arbitrarily selected streamwise–wall-normal transects of high-Re_τ flows, outer-layer coherence in turbulent wall flows manifests as inclined parcels of quasi-uniform momentum – relative deficits and excesses about the mean – all of which are bound by interfacial shear zones. These so-called uniform momentum zones (UMZs) have been observed in numerous experiments (Meinhart & Adrian 1995), and more recent efforts have further augmented understanding of UMZs (de Silva *et al.* 2017; Bautista *et al.* 2019; Heisel *et al.* 2020). Prior observations have generally been based on experimental measurements, but for this study we leverage the opportunity afforded by a recent direct numerical simulation (DNS) modelling campaign of channel flow up to $Re_\tau = 5200$ (Lee & Moser 2015, 2019). Data for this case are used to simultaneously explore the inner–outer-layer dynamics and to demonstrate an underlying similarity in the interfacial shear between successive UMZs.

Table 1 provides a summary of the DNS cases, where for this work the Cartesian vector, $\boldsymbol{x}^+ = \{x_1^+, x_2^+, x_3^+\}$, and the first, second and third components of any vector correspond to constituent magnitudes in the streamwise, spanwise and wall-normal directions, respectively. Thus, in table 1, L_1/δ and L_2/δ are the outer-normalized streamwise and spanwise spatial extents, respectively, of the computation domain; δ_1^+ and δ_2^+ are the inner-normalized streamwise and spanwise grid resolutions; $\delta_3^+|_w$ and $\delta_3^+|_c$ are the inner-normalized wall-normal grid resolutions used within the B-spline grid discretization at the wall and centreline, respectively (Lee & Moser 2015, 2019). The computational meshes were discretized with N_1, N_2 and N_3 compute points in the streamwise, spanwise and wall-normal directions, respectively, while Tu_τ/δ is the simulation time. Comprehensive simulation details are available in Lee & Moser (2015, 2019).

Analysis of the high-Re_τ results clearly show the presence of UMZs, while more in-depth processing will show that the interfacial shear between successive UMZs induces gradients which do not scale in the wall-normal direction as $(x_3^+)^{-1}$, as predicted by the attached-eddy paradigm and associated logarithmic dependence of velocity upon x_3^+; rather, we will demonstrate that vertical gradients systematically decrease at the relatively slower rate, $(x_3^+)^{-1/2}$. This is recovered from assessment of inner-normalized Kolmogorov length. Further processing of the vertical gradient of streamwise velocity and vorticity thickness confirm this wall-normal dependence. Herein, we propose that UMZs are the product of bluff-body-like interactions in the inner layer, which induce wakes that emanate through the outer layer. Following Tennekes & Lumley (1972), the streamwise momentum equation is posed in similarity form for a wake, yielding wall-normal scaling for the vorticity thickness, velocity gradients and Kolmogorov length, in agreement with the results from high-Re_τ DNS.

Case	Re_τ	L_1/δ	L_2/δ	δ_1^+	δ_2^+	$\delta_3^+|_w$	$\delta_3^+|_c$	N_1	N_2	N_3	Tu_τ/δ
C1	182	8π	3π	4.467	3.352	1.054×10^{-2}	3.059	1024	512	192	31.9
C2	544	8π	3π	8.901	5.007	2.7×10^{-3}	4.528	1536	1024	384	13.6
C3	1000	8π	3π	10.908	4.602	2.765×10^{-3}	6.224	2304	2048	512	12.5
C4	1995	8π	3π	12.241	6.117	2.428×10^{-3}	8.2345	4096	3072	768	11.5
C5	5185	8π	3π	12.726	6.363	7.110×10^{-2}	10.347	10 240	7680	1536	7.8

TABLE 1. Summary of DNS case details, where far right-hand column denotes outer-normalized simulation time; vertical (x_3^+) computational mesh spacing based upon B-spline discretization, where $\delta_3^+|_w$ and $\delta_3^+|_c$ denote wall and centreline grid spacings, respectively. For comprehensive details, see Lee & Moser (2015).

2. Results from DNS of high-Re_τ channel flow

Figure 1 shows streamwise velocity, u_1^+, at an arbitrary time and in a series of formats for Case C5 (for this work, fluctuations are denoted as deviations from the Reynolds average, $\boldsymbol{u}' = \boldsymbol{u} - \langle\boldsymbol{u}\rangle_t$, where $\langle\cdots\rangle_a$ denotes averaging over dimension a; where noted, we leverage the horizontal homogeneity of channels and use the plane average as an interchangeable surrogate for the time average). In figure 1 and all subsequent figures, blue lines at fixed values of x_3^+ denote the lower and upper limit of the logarithmic layer, as per reference material provided in Pope (2000). Panel (*a*) shows a colour flood contour of $u_1^{+,\prime}$, where yellow lines denote structural inclination angle, $\gamma = 16°$, for large-scale motions (Hutchins & Marusic 2007). The contours reveal the 'staircase-like' pattern of successive UMZs (Heisel *et al.* 2020), where the intensity of successive UMZs (momentum excess or deficit) diminishes with x_3^+ increasing. In order to simultaneously assess the inner- and outer-layer dynamics, panel (*b*) shows isocontours of $u_1^{+,\prime} = +1$ (black) and -1 (grey) over the region denoted in panel (*a*). The panel (*b*) ordinate is shown in logarithmic scale, which reveals the presence of inner-layer regions of momentum excess and deficit (Jimenez & Pinelli 1999; Schoppa & Hussain 2002). Panel (*b*) constitutes preliminary evidence of the inner-layer bluff-body-like dynamics creating wakes that emanate into the outer layer, which manifest as UMZs. The region, $x_1^+ \approx 6.7 \times 10^4$ and $\approx 9.0 \times 10^4$ and $x_3^+ \approx 50$, marks the location of two example bluff-body-like interactions, where parcels of momentum excess encounter parcels of momentum deficit, inducing the wake-like parcels of fluid which conform to the inclination lines superimposed upon the panels.

Panels (*c–g*) show u_1^+ at the series of streamwise locations denoted in panel (*a*) by vertical black lines, where panels (*c–g*) correspond to monotonically increasing x_1^+ locations. The logarithmic law is superimposed upon the panels, for reference, while clear UMZs were visually detected and are highlighted with annotations (more sophisticated UMZ identification methods are available, but this is not the purpose of the present paper; Fan *et al.* 2019). The observed UMZs in panels (*c–g*) correlate with the intersection of parcels of quasi-uniform momentum in panel (*a*): consider, for example, the momentum deficits at $x_1^+ \approx 3 \times 10^4$ (*d*) and $\approx 3.5 \times 10^4$ (*e*), or the momentum excesses at $x_1^+ = 8 \times 10^4$ (*f*) and $\approx 11.5 \times 10^4$ (*g*). The existence of these UMZs necessitates relatively large interfacial gradients. One such way to record this is through consideration of the turbulent kinetic energy (k) balance and the Kolmogorov length.
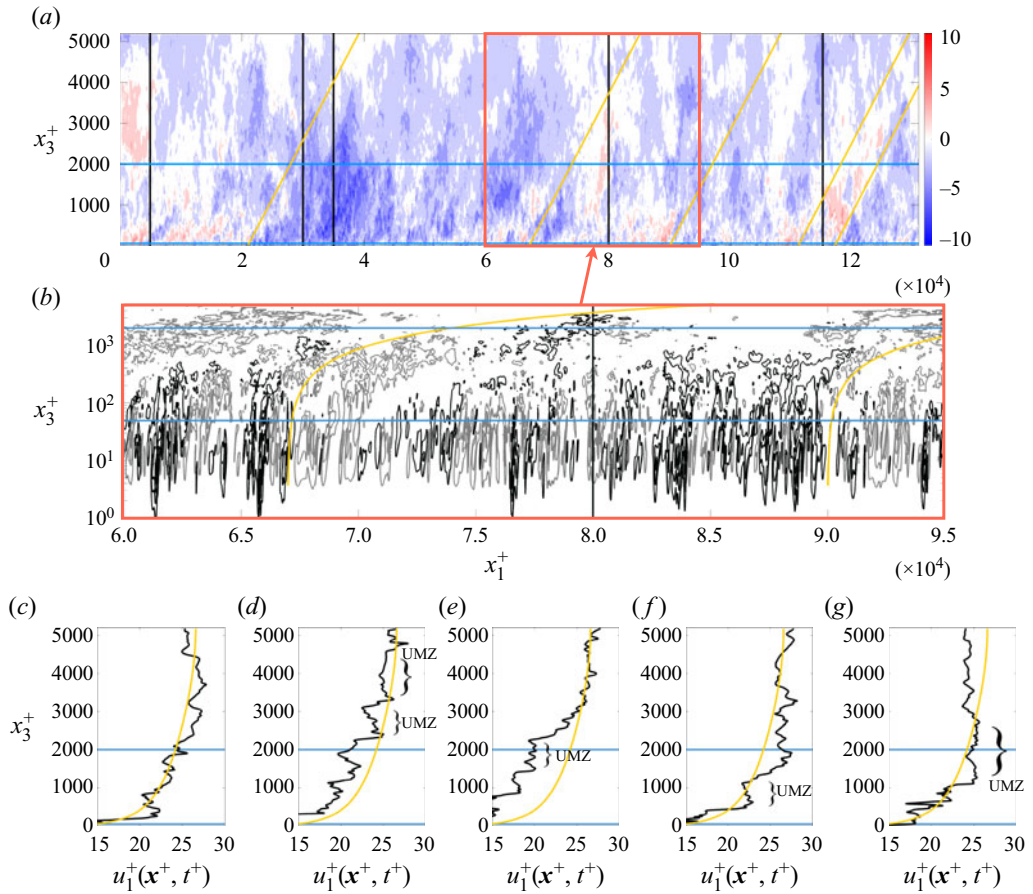
FIGURE 1. Instantaneous streamwise velocity from DNS of channel flow at $Re_\tau = 5200$ (Case C5, table 1). Panels (a,b) show fluctuating streamwise velocity, $u_1^{+,\prime}$ linear and logarithmic ordinate scalings, respectively, where panel (b) corresponds with the relatively lesser streamwise extent indicated in panel (a). Solid black and grey lines in panel (b) denote $u_1^{+,\prime} = 1.0$ and -1.0, respectively; inclined yellow lines in panels (a,b) denote inclination line, $\gamma = 16°$, which is typical of inclined inertial-layer structures (Adrian *et al.* 2000; Hutchins & Marusic 2007). Panels $(c–g)$ show $u_1^{+,\prime}$ at the five streamwise locations denoted by vertical black lines in panel (a), where annotations are superimposed to highlight UMZs through visual inspection. In panels $(c–g)$, the yellow profile denotes the logarithmic velocity profile (2.3a,b), while upper and lower horizontal blue lines in panels $(b–g)$ denote the base and ceiling of the logarithmic layer, respectively, as per reference material provided in Pope (2000).

For the cases recorded in table 1, figure 2(a) shows vertical profiles of plane- and time-averaged k production (gain) and dissipation (loss), respectively, where $\langle \mathcal{P}^+ \rangle_{12t} = \langle u^{+,\prime} \otimes u^{+,\prime} : \nabla^+ \langle u^+ \rangle_t \rangle_{12t}$ and $\langle \epsilon^+ \rangle_{12t} = \langle \nabla^+ u^{+,\prime} : \nabla^+ u^{+,\prime} \rangle_{12t}$. Annotations are superimposed upon panel (a) to indicate the direction of increasing Re_τ, which corresponds to a monotonically increasing magnitude of dissipation and production in the inner layer. The dissipation profiles can be used to recover the inner-normalized Kolmogorov length, $\eta^+ = (\epsilon^+)^{-1/4}$, where figure 2(b) shows profiles for Cases C1 to C5. Panel (b) indicates that η^+ exhibits three distinct regimes of dependence upon x_3^+, where the regions of
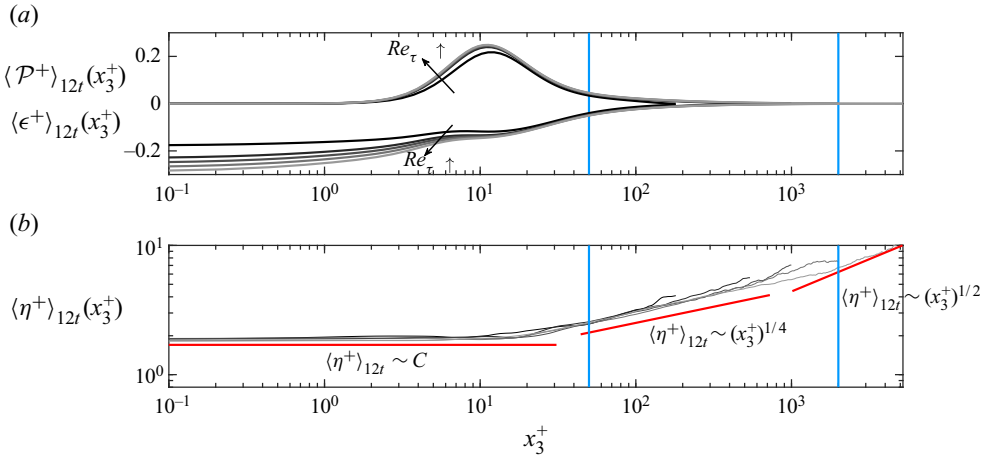
FIGURE 2. Turbulence statistics from DNS of channel turbulence. Panel (*a*) shows vertical profiles of plane- and time-averaged inner-normalized production and dissipation, with direction of Re_τ increasing superimposed for perspective. Panel (*b*) shows vertical profiles of inner-normalized Kolmogorov length, with models superimposed showing elevations of validity for different scaling arguments. In both panels, black to light grey profiles correspond to Cases C1 to C5, see table 1.

validity are noted below:

$$\left.\begin{array}{l} \langle \eta^+ \rangle_{12} \sim C \quad \text{for } x_3^+ \lesssim 20 \\ \langle \eta^+ \rangle_{12} \sim (x_3^+)^{1/4} \quad \text{for } 20 \lesssim x_3^+ \lesssim \lambda, \quad \text{and} \\ \langle \eta^+ \rangle_{12} \sim (x_3^+)^{1/2} \quad \text{for } x_3^+ \gtrsim \lambda, \end{array}\right\} \tag{2.1}$$

where λ is the elevation at which the logarithmic-layer scaling transition occurs. Inspection of figure 2(*b*) indicates that $\lambda \approx Re_\tau/2$ (discussion to follow). With the exception of $d_{3^+} \langle u_1^+ \rangle_{12t}(x_3^+)$, all other components of the Reynolds-averaged velocity gradient tensor vanish for a channel; this attribute provides a benchmark for assessment of the Kolmogorov length profiles shown in figure 2(*b*) and the equation (2.1) results. Within the inner (viscous wall) layer,

$$\langle u_1^+ \rangle_{12t}(x_3^+) = x_3^+ \quad \text{for } x_3^+ \lesssim 50, \quad \text{and} \quad d_{3^+} \langle u_1^+ \rangle_{12t}(x_3^+) = 1, \tag{2.2a,b}$$

while in the logarithmic layer, the form of $\langle u_1^+ \rangle_{12t}(x_3^+)$ changes

$$\langle u_1^+ \rangle_{12t}(x_3^+) = \frac{1}{\kappa} \log(x_3^+) + A \quad \text{for } x_3^+ \gtrsim 50, \quad \text{and} \quad d_{3^+} \langle u_1^+ \rangle_{12t}(x_3^+) = (\kappa x_3^+)^{-1}. \tag{2.3a,b}$$

Thus, the inner- and logarithmic-layer estimates for velocity agree, but the intermediate argument, $\langle \eta^+ \rangle_{12} \sim (x_3^+)^{1/4}$, cannot be explained by either. It is emphasized that the scaling arguments superimposed upon figure 2(*b*) are based only on a fit (solid red lines), and not from any order-or-magnitude analysis of governing transport equations, etc.

The results presented in figure 2 indicate the presence of a layer that cannot be attributed to the viscous sublayer or logarithmic layer. Herein, we will demonstrate that this non-conforming scaling is the product of elevated shear associated with the
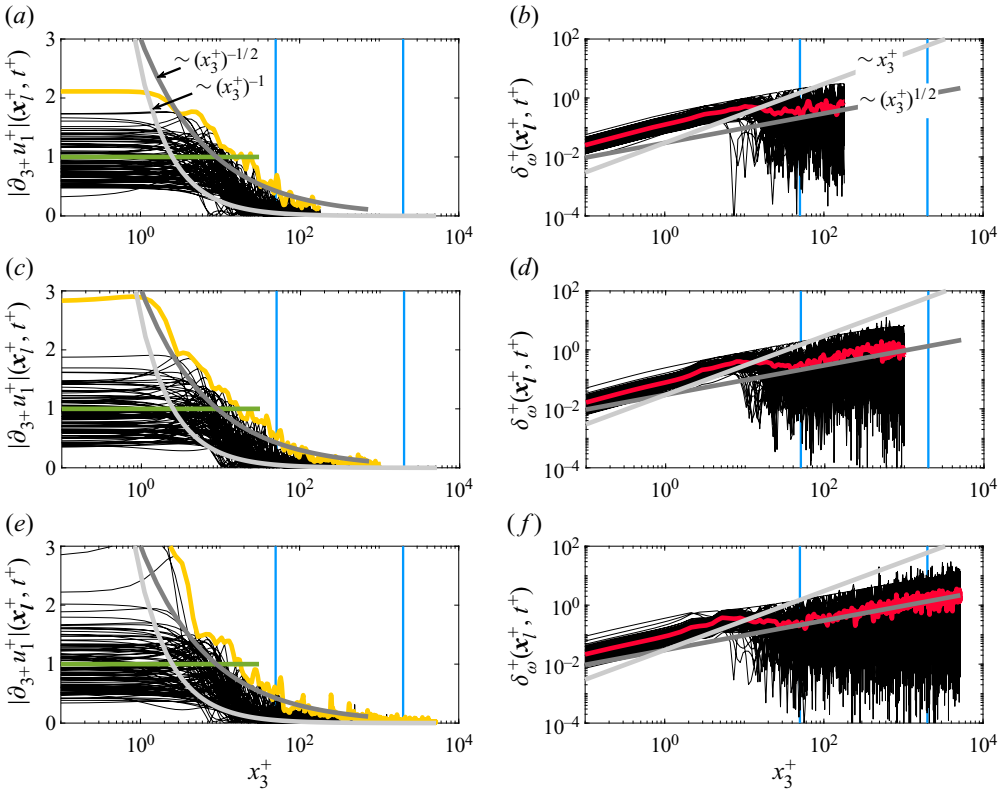
FIGURE 3. Vertical profiles of instantaneous absolute value of vertical gradient of streamwise velocity (*a,c,e*) and vorticity thickness (*b,d,f*; (2.4)) at arbitrarily selected streamwise–spanwise locations throughout the computational domain. Results shown for Case C1 (*a,b*), C3 (*c,d*) and C5 (*e,f*), with intermediate cases omitted for brevity. In (*a,c,e*), yellow profiles correspond to the maximum value of $|\partial_{3^+} u_1^+|$ reported at each elevation, horizontal green lines correspond to analytical inner-layer gradient (2.2*a,b*). Solid light and dark grey lines correspond to analytical logarithmic-layer gradient (2.3*a,b*) and scaling argument recovered from the Kolmogorov length (figure 2*b*); annotations for both superimposed in panel (*a*). Solid red line in (*b,d,f*) indicates averaged vorticity thickness at each elevation; solid light and dark grey lines correspond to idealized scaling upon x_3^+ based upon logarithmic law and Kolmogorov length profiles, with annotations both superimposed in panel (*b*).

passage of UMZs, for which the wall-normal gradient of streamwise velocity provides the dominant contribution. The following results, and subsequent self-similar UMZ interfacial wakes behaving as canonical wakes, are all entirely consistent with this result. In the interest of brevity, a component-by-component analysis is not presented here – i.e. $\langle (\partial_{1^+} u_1^+)^{-1/4} \rangle_{12t}(x_3^+)$, etc. – and we direct the interested reader to the Appendix.

Figure 3 shows arbitrarily selected vertical profiles of $|\partial_{3^+} u_1^+|$ (left column) and vorticity thickness,

$$\delta_\omega^+(x_3^+) = \frac{\delta u_1^+}{\underbrace{max}_{12}(|\partial_{3^+} u_1^+|)}, \qquad (2.4)$$

in the right column, where $\delta u_1^+ = u_1^+(x_{1,l}^+, x_{2,l^+}^+, x_{3,l}^+ + \delta_3^+, t^+) - u_1^+(x_{1,l}^+, x_{2,l}^+, x_{3,l}^+, t^+)$, $\boldsymbol{x}_l^+$ corresponds to the locations at which individual profiles are taken, δ_3^+ is the wall-normal computational mesh resolution (table 1 and accompanying text) and 12 beneath the '*max*' operation denotes maximum in the x_1–x_2 plane; after de Silva *et al.* (2017), we define vorticity thickness in terms of the maximum gradient. Since successive UMZs are composed of differing aggregate momentum, the instantaneous wall-normal gradient of streamwise velocity can be negative. In order to focus the present article on the magnitude of interfacial shear, the absolute value of the gradient, $|\partial_{3^+} u_1^+|$, is used in (2.4). Profiles for Cases C2 and C4 are omitted from figure 3 for brevity, although we report monotonic variation of the relevant quantities with Re_τ. For the purpose of figure 3, profiles are selected arbitrarily. In panels (*a,c,e*), the solid green and light grey lines correspond to the gradients predicted by (2.2*a,b*) and (2.3*a,b*), respectively, while the solid yellow line is the maximum value recorded at each location ((2.4) denominator); the solid dark grey line denotes $|\partial_{3^+} u_1^+| \sim (x_3^+)^{-1/2}$. Panel (*a*) includes annotation for the outer-layer x_3^+ dependencies reported. It is clear that, instantaneously, the wall-normal gradients decline slower (in space) than would otherwise be predicted by the logarithmic law, which is the signature of elevated shear within the interfacial zones between successive UMZs. This is evidenced by overlap between the dark grey and yellow profiles, indicating that elevated interfacial gradients cannot possibly be attributed to equilibrium condition shear; UMZ shear exhibits a predictable form. Provided Re_τ is sufficiently large, this trend occurs continuously, with $|\partial_{3^+} u_1^+| \sim (x_3^+)^{-1/2}$ agreeing with the maximum gradient for $20 \lesssim x_3^+ \lesssim \lambda$ (see also figure 2*b*).

Figure 3(*b,d,f*) shows arbitrarily selected profiles $\delta_\omega^+(\boldsymbol{x}_l^+, t^+)$ (2.4), where panel (*b*) includes annotations for the additional profiles; it is self-evident that the velocity gradient and vorticity thickness are inversely related: the red profiles in panels (*b,d,f*) are $\langle \delta_w^+ \rangle_{12}(x_3^+, t)$, and it is immediately apparent that this quantity exhibits $\langle \delta_w^+ \rangle_{12}(x_3^+, t) \sim (x_3^+)^{1/2}$. Others have considered the vorticity thickness associated with the interfacial layers (de Silva *et al.* 2017; Bautista *et al.* 2019), but the current wall-normal scaling confounds description within the attached-eddy paradigm of the outer layer. In the following section, the results presented herein will be interpreted in the context of a wake model, wherein successive UMZs originate from bluff-body-like inner-layer interactions between fluid parcels of differing age and aggregate momentum (Adrian *et al.* 2000). This is sketched in figure 4, which presents an idealized depiction of the inner-layer collision between a relatively faster parcel (red) and relatively slower parcel (blue), necessarily leading to the interfacial wake zone (grey) and momentum defect; the figure includes annotation for the inclination angle, γ, and readers will note conceptual similarity between figure 4 and 1(*b*). The momentum parcels illustrated in figure 4 manifest as UMZs when measured at a fixed streamwise–spanwise location, thereby leading to the 'staircase-like' increases in velocity with increasing x_3^+ (Meinhart & Adrian 1995; de Silva *et al.* 2017; Bautista *et al.* 2019; Heisel *et al.* 2020). In the following section, wake-scaling arguments are used to recover wall-normal dependence of the velocity gradients across UMZ interfaces.

3. Wake model for UMZ evolution

The interfacial zones between successive UMZs are envisioned as a series of recovering wakes. Consider the inner-scaled momentum transport equation, absent spanwise transport effects

$$\langle \boldsymbol{u}_1^+ \rangle_t \cdot \nabla^+ \langle u_1^+ \rangle_t + \nabla^+ \cdot \langle \boldsymbol{u}^{+,\prime} \otimes u_1^{+,\prime} \rangle_t = -\partial_1^+ P_0^+ + (\nabla^+)^2 \langle u_1^+ \rangle_t, \tag{3.1}$$
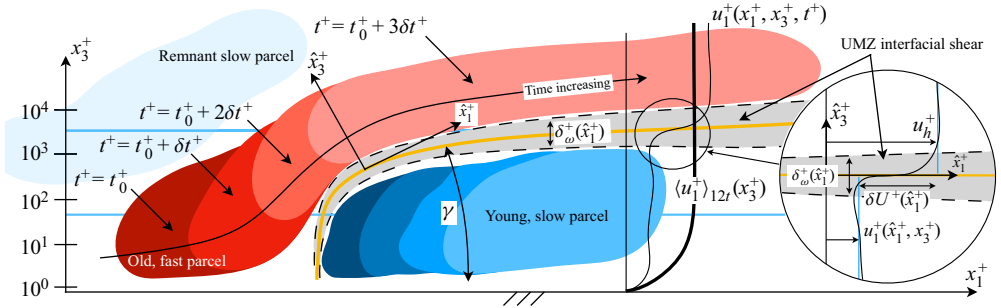
FIGURE 4. Conceptual schematic of dynamical and hierarchical nature of hairpin packets (Adrian *et al.* 2000) originating within inner layer and emanating into outer layer. Dark to light parcels of red and blue correspond to successive realizations of a relative streamwise momentum excess and deficit at a series of successive times (annotations provided in panel), which manifest at later times as UMZs. Yellow line denotes inclination angle (see also figure 1*a*,*b*), which sets the origin of a local Cartesian coordinate system, $\hat{x}^+ = \{\hat{x}_1^+, \hat{x}_3^+\}$. Grey region denotes interfacial shear between vertically adjacent UMZs, with vorticity thickness shown and idealized instantaneous (thin solid black) and Reynolds-averaged (thick solid black) streamwise velocity shown. Inset shows vorticity thickness and wake deficit. Superimposed upon the panel is a yet-older parcel of streamwise momentum deficit (light blue).

where viscosity is embodied within the inner-scaled dimensions and total pressure, $P_0^+ = P/(\rho u_\tau^2) + \langle u_3^+ \rangle_t^2$, where P is mechanical pressure (discussion to follow for application to turbulent wakes). The momentum deficit between vertically adjacent UMZs, $\delta U^+(\boldsymbol{x}^+)$, and the vorticity thickness, $\delta_\omega^+(\boldsymbol{x}^+)$, constitute salient normalizing scales for (3.1). As will be shown in subsequent developments, these normalizing quantities will not preclude dependence upon x_3^+. Owing to scaling arguments of wakes, for which $\boldsymbol{u}^{+,\prime}/\delta U = O(10^0)$, divergence of the normal (turbulent) stresses and all right-hand side terms vanish from (3.1). For the present application to UMZs, the imposed pressure gradient is eliminated, $\partial_1^+ P_0^+ \to 0$, while order-of-magnitude arguments show that $\partial_1^+ \langle u_3^+ \rangle_t^2 = -\partial_1^+ P^+ \to 0$; given that comprehensive details of these developments are available in a benchmark turbulence reference (Tennekes & Lumley 1972), additional information is left to the interested reader. After Tennekes & Lumley (1972), it follows that the problem can be posed in self-preserving similarity form by adopting a model of UMZs as wakes originating from the inner-layer interactions between relatively young, slow parcels and relatively old, fast parcels (figure 4). For descriptive purposes, a local coordinate system is introduced, $\hat{\boldsymbol{x}}^+ = \{\hat{x}_1^+, \hat{x}_3^+\}$, which is shown in figure 4; this coordinate system represents an idealized depiction of the evolving interface between two parcels of fluid, and we emphasize that the perception of a curved mapping is a product of the logarithmic–linear axis scaling (see also figure 1*b*). Owing to the aforementioned reductions to (3.1), a self-preserving similarity form requires only models for streamwise velocity and the streamwise–wall-normal turbulent stresses; in the inclined coordinate system, these are

$$\frac{u_h^+ - \langle u_1^+ \rangle_t(\hat{x}_1^+, \hat{x}_3^+)}{\delta U^+(\hat{x}_1^+)} = f(\eta) \quad \text{and} \quad \frac{\langle u_1^{+,\prime} u_3^{+,\prime} \rangle_t}{(\delta U^+(\hat{x}_1^+))^2} = -g(\eta), \quad \text{where } \eta = \frac{\hat{x}_3^+}{\delta_\omega^+(\hat{x}_1^+)}, \tag{3.2a,b}$$

where u_h^+ is the 'high' velocity above the wake (see also figure 4). Following application of the aforementioned conditions and substitution of the similarity-form streamwise velocity

and turbulent stresses, (3.1) becomes

$$u_h^+ \left(\frac{\delta U^+}{\delta_\omega^+} (\partial_{1+}\delta_\omega^+)\eta \, \mathrm{d}_\eta f - (\partial_{1+}[\delta U^+])f \right) = \mathrm{d}_\eta g = Re_T^{-1} \, \mathrm{d}_\eta^2 f, \tag{3.3}$$

where $Re_T = \delta U^+ \delta_\omega^+ / \nu_T$, and it is noted that the Reynolds (turbulent) stress divergence term has been reconciled with velocity via the incompressible Boussinesq model (Pope 2000); with this, the turbulent stresses are expressed alternatively: $\langle u_1^{+,\prime} u_3^{+,\prime} \rangle_t = -(\delta U^+(\hat{x}_1^+))^2 g(\eta) = -\nu_T \partial_{3+} u_1^+$. Note, too, that the remaining advective term simplifies

$$\langle u_1^+ \rangle_t \partial_{1+} \langle u_1^+ \rangle_t = u_h^+ \partial_{1+} \langle u_1^+ \rangle_t - \delta U^+ f \partial_{1+} \langle u_1^+ \rangle_t \rightarrow u_h^+ \partial_{1+} \langle u_1^+ \rangle_t, \tag{3.4}$$

since $\delta U^+ / u_h^+ \sim O(\delta_\omega^+ / \hat{x}_1^+)$, and the advective velocity embodied by each successive UMZ is expressed relative to its predecessor (Tennekes & Lumley 1972). The following conditions are necessary for the existence of self-preserving wakes

$$\left. \begin{aligned} \delta_\omega^+ (\delta U^+)^{-2} \partial_{1+} \delta U^+ = \mathcal{A} = \text{constant}, \\ (\delta U^+)^{-1} \partial_{1+} \delta_\omega^+ = \mathcal{B} = \text{constant} \quad \text{and} \\ Re_T = \text{constant}. \end{aligned} \right\} \tag{3.5}$$

We follow Tennekes & Lumley (1972) by adopting the general conditions, $\delta_\omega^+ \sim (\hat{x}_1^+)^n$ and $\delta U^+ \sim (\hat{x}_1^+)^m$, where the requirements imposed by (3.5) yield the undetermined system, $m = n - 1$, indicating the need for an additional constraint. After Tennekes & Lumley (1972), one such constraint can conveniently be recovered from the integral-form streamwise momentum transport equation,

$$\int_{-\infty}^{\infty} \langle u_1^+ \rangle_t (\langle u_1^+ \rangle_t - u_h^+) \mathrm{d}\hat{x}_{3+} = -(u_h^+)^2 \theta, \tag{3.6}$$

where θ is the momentum thickness (note that terms of order, $\delta U^+ / u_h^+$, are eliminated from the integral since they are vanishingly small). With this, substitution of the self-preservation form model for $\langle u_1^+ \rangle_t$ (3.2a,b) yields,

$$\delta U^+ \delta_\omega^+ \left(\int_{-\infty}^{\infty} f \, \mathrm{d}\eta - \frac{\delta U^+}{u_h^+} \int_{-\infty}^{\infty} f^2 \, \mathrm{d}\eta \right) = -u_h^+ \theta, \tag{3.7}$$

thereby providing a means to close the system: since $\rho^{-1} \, \mathrm{d}_{\hat{1}+} M_{\hat{1}+} = -\mathrm{d}_{\hat{1}+}((u_h^+)^2 \theta) = 0$ – where $M_{\hat{1}+}$ is streamwise momentum and ρ is fluid density – $u_h^+ \theta$ is necessarily constant, and (3.7) necessitates that $\delta U^+ \delta_\omega^+ \sim (\hat{x}_1^+)^n (\hat{x}_1^+)^{n-1}$ must also be constant; with this, we recover the results already presented by Tennekes & Lumley (1972)

$$\delta U^+ \sim (\hat{x}_1^+)^{-1/2} = \mathcal{A}_1 (\hat{x}_1^+)^{-1/2} \quad \text{and} \quad \delta_\omega^+ \sim (\hat{x}_1^+)^{1/2} = \mathcal{A}_2 (\hat{x}_1^+)^{1/2}. \tag{3.8a,b}$$

The proportionality constants, $\mathcal{A}_1$ and $\mathcal{A}_2$, needed in (3.8a,b), can be recovered via subsequent rudimentary developments. The result for δ_ω^+ is consistent with the scaling recovered from the DNS data (figure 3b,d,f), which showed a pronounced region of $\delta_\omega^+ \sim (x_3^+)^{1/2}$. The result is also physically intuitive: the velocity defect and vorticity thickness
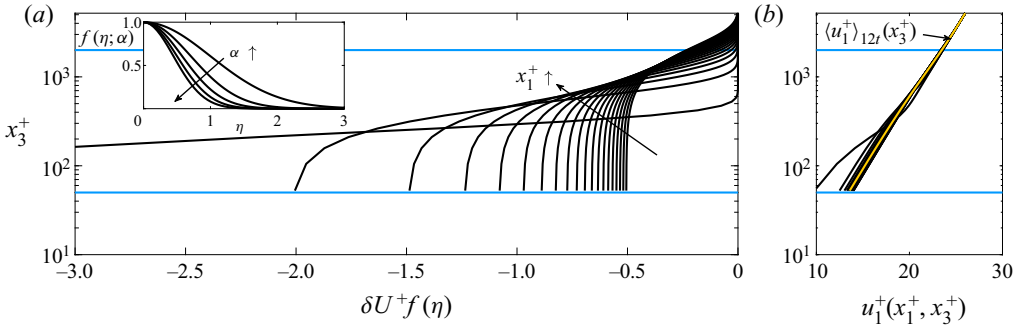
FIGURE 5. Results of wake model (*a*) and application to modelling logarithmic layer (*b*). Panel (*a*) shows wake profile, $u_1^+ = \delta U^+ f(\eta)$, at a series of increasing streamwise locations, which for a channel are the conceptual equivalent of increasing time; inset shows self-preserving similarity-form wake deficit profile (3.10). Panel (*b*) shows instantaneous streamwise velocity with wake deficit profile and outer velocity modelled as per (3.13).

must decrease and increase, respectively, for increasing $\hat{x}_1^+$. With further developments, it can be shown that (3.3) reduces to

$$f'' + \alpha \left(\eta f' + f\right) = 0, \tag{3.9}$$

where $\alpha = (1/2) Re_T u_h^+ (\mathcal{A}_1/\mathcal{A}_2)$; the solution to (3.9) has the form,

$$f(\eta; \alpha) = \exp\left(-\tfrac{1}{2}\alpha\eta^2\right), \tag{3.10}$$

where a series of profiles for $f(\eta; \alpha)$ are shown in figure 5(*a*, inset), while panel (*a*) itself shows the momentum defect, $\delta U^+ f$, for $\mathcal{A}_1 \to 1$ at a series of streamwise locations. The quantity is shown against x_3^+, which is enabled by the linear mapping from $\hat{x}_1^+$ to x_3^+ afforded by the oblique-aligned Cartesian coordinate systems and the *a priori* defined proportionality constant, $\mathcal{A}_1$. Owing to the similarity variable (3.2*a,b*), $\delta U^+ f$ correctly captures the diminishing defect for increasing values of x_1^+ and x_3^+. In addition to the correct scaling arguments already shown by (3.8*a,b*), note also that the preceding developments enable recovery of the vertical dependence of the vertical gradient

$$\partial_{\hat{3}^+} u_1^+ = -\left(\partial_{\hat{3}^+}(\delta U^+) f - \delta U^+ \partial_{\hat{3}^+} f\right) = \left(\alpha \frac{\delta U^+}{(\delta_\omega^+)^2} \hat{x}_3^+ - \partial_{\hat{3}^+}\delta U^+\right) f, \tag{3.11}$$

where the second term within the far right-hand side term vanishes upon factorization of the entire term by $\hat{x}_3^+/\delta_\omega^+$. Following substitution of the $\hat{x}_3^+$ scaling arguments already established in the preceding developments (3.8*a,b*), it can be shown that

$$\partial_{\hat{3}^+} u_1^+ \to \alpha \frac{\delta U^+}{(\delta_\omega^+)^2} \hat{x}_3^+ f \sim \frac{(\hat{x}_3^+)^{-1/2}}{\hat{x}_3^+} \hat{x}_3^+ \sim (\hat{x}_3^+)^{-1/2} \sim (x_3^+)^{-1/2}, \tag{3.12}$$

in accordance with the results already shown (figures 2*b* and 3*a,c,e*); it is noted, also, that while the preceding development was posed in terms of the $\boldsymbol{x}^+ = \{\hat{x}_1^+, \hat{x}_3^+\}$ vector space, which was oblique to the $\boldsymbol{x}^+ = \{x_1^+, x_3^+\}$ vector space by inclination angle, γ, the scaling arguments are equally valid since both coordinate systems are Cartesian.

As a final remark, it is worth considering how the arguments presented herein yield $d_{3^+} \langle u_1^+ \rangle_{12t}(x_3^+) \sim (x_3^+)^{-1}$, where $\langle u_1^+ \rangle_{12t}$ is the Reynolds-averaged streamwise velocity. That is, if the inclined wake model correctly represents instantaneous flow states, its Reynolds average should nevertheless recover the logarithmic law when averaged over a sufficient number of ensembles. This condition is leveraged as a means to define u_h^+, since

$$\langle u_1^+ \rangle_{12t} = \langle u_h^+ \rangle_{12} - \langle \delta U^+ f \rangle_{12t} \to \frac{1}{\kappa} \log(x_3^+) + A, \qquad (3.13)$$

where $\langle \delta U^+ f \rangle_{12t} \to 0$ is a natural consequence of the fluctuating nature of successive UMZs. In adopting this approach, the streamwise-heterogeneous component within the model for streamwise velocity, $\delta U^+ f(\eta)$ (3.2*a,b*), encompasses the effects of time dependence for the case of a channel. This tendency towards the logarithmic law in a Reynolds-averaged sense is tantamount to the aforementioned Re_τ dependence upon $\langle \eta^+ \rangle_{12t}$, where we observed scaling transition at $\lambda \approx Re_\tau/2$. Physical support for this transition elevation, and dependence upon λ, will be the topic of future work.

4. Concluding remarks

Recent experiments have confirmed that the inertial layer of high-Re_τ boundary layers are dominated by UMZs (Meinhart & Adrian 1995; de Silva *et al.* 2017; Bautista *et al.* 2019; Heisel *et al.* 2020). These inclined regions of quasi-uniform momentum manifest as a 'staircase-like' pattern when recorded at a fixed streamwise–spanwise location. The intensity of UMZs attenuates with increasing wall-normal direction. For this work, high-Re_τ DNS of channel flow is used to quantify the influence of strong interfacial shear between successive UMZs: results show that this interfacial shear contributes to non-logarithmic scaling of instantaneous streamwise velocity, which subsequently affects the wall-normal dependence of the velocity gradient and vorticity thickness. The DNS results afford simultaneous consideration of the inner- and outer-layer processes, which are used to develop a conceptual description of UMZs as the product of inner-layer bluff-body-like interactions. When viewed in this way, the associated momentum defect and turbulent stresses can be posed in self-similar form to recover wall-normal dependence of the velocity gradient. Agreement between predictions from the similarity solution and DNS results establishes support for the notion of UMZs as wakes emanating from inner-layer dynamics.

Declaration of interests

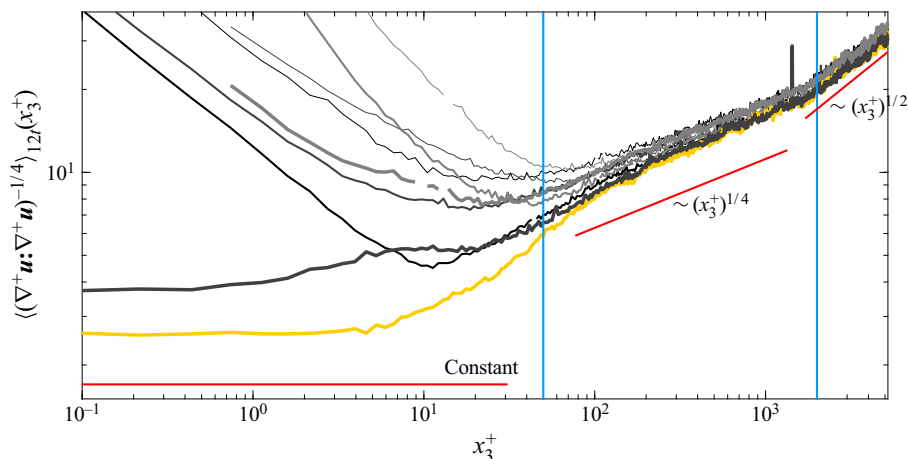The authors report no conflict of interest.

FIGURE 6. Vertical profiles of Kolmogorov length due to discrete components of the velocity gradient tensor, averaged in the streamwise, spanwise and time dimensions. Profiles correspond to contributions due to streamwise gradients (thin lines), spanwise gradients (intermediate line thickness) and vertical gradients (thick lines) of streamwise velocity (black), spanwise velocity (grey) and vertical velocity (light grey); note that $\langle (\partial_{3^+} u_1^+)^{-1/4} \rangle_{12t}(x_3^+)$ is denoted by an amber profile, for emphasis. Also superimposed are scaling relations used in figure 2. Profiles shown for Case C5, see table 1.

Appendix

It is argued throughout that $\langle (\partial_{3^+} u_1^+)^{-1/4} \rangle_{12t}(x_3^+)$ makes the dominant contribution for the Kolmogorov length, with the resulting scaling results used to argue that this shear is the marker of UMZ interfacial shear. In order to demonstrate efficacy of this assumption, figure 6 shows vertical profiles of Kolmogorov length due to constituent components of the velocity gradient tensor, with colour- and line-coding definitions provided in the definition. Here, $\langle (\partial_{3^+} u_1^+)^{-1/4} \rangle_{12t}(x_3^+)$ is denoted by an amber line, which confirms that the Kolmogorov length is smallest – due to the strongest shear – for this component.

REFERENCES

ADRIAN, R. J., MEINHART, C. D. & TOMKINS, C. D. 2000 Vortex organization in the outer region of the turbulent boundary layer. *J. Fluid Mech.* **422**, 1–54.

BAUTISTA, J. C. C., EBADI, A., WHITE, C. M., CHINI, G. P. & KLEWICKI, J. C. 2019 A uniform momentum zone–vortical fissure model of the turbulent boundary layer. *J. Fluid Mech.* **858**, 609–633.

FAN, D., XU, J., YAO, M. X. & HICKEY, J.-P. 2019 On the detection of internal interfacial layers in turbulent flows. *J. Fluid Mech.* **872**, 198–217.

HEISEL, M., DE SILVA, C. M., HUTCHINS, N., MARUSIC, I. & GUALA, M. 2020 On the mixing length eddies and logarithmic mean velocity profile in wall turbulence. *J. Fluid Mech.* **887**, R1.

HUTCHINS, N & MARUSIC, I 2007 Evidence of very long meandering features in the logarithmic region of turbulent boundary layers. *J. Fluid Mech.* **579**, 1–28.

JIMENEZ, J. & PINELLI, A. 1999 The autonomous cycle of near-wall turbulence. *J. Fluid Mech.* **389**, 335–359.

LEE, M. & MOSER, R. D. 2015 Direct numerical simulation of turbulent channel flow up to $Re_\tau = 5200$. *J. Fluid Mech.* **774**, 395–415.

LEE, M. & MOSER, R. D. 2019 Spectral analysis of the budget equation in turbulent channel flows at high Reynolds number. *J. Fluid Mech.* **860**, 886–938.

MARUSIC, I., MATHIS, R. & HUTCHINS, N. 2010 Predictive model for wall-bounded turbulent flow. *Science* **329**, 193–196.

MEINHART, C. D. & ADRIAN, R. J. 1995 On the existence of uniform momentum zones in a turbulent boundary layer. *Phys. Fluids* **7**, 694–696.

POPE, S. B. 2000 *Turbulent Flows*. Cambridge University Press.

SCHOPPA, W. & HUSSAIN, F. 2002 Coherent structure generation in near-wall turbulence. *J. Fluid Mech.* **453**, 57–108.

DE SILVA, C. M., PHILIP, JIMMY, HUTCHINS, N. & MARUSIC, I. 2017 Interfaces of uniform momentum zones in turbulent boundary layers. *J. Fluid Mech.* **820**, 451–478.

TENNEKES, H. & LUMLEY, J. L. 1972 *A First Course in Turbulence*. MIT Press.